Rotor Interaction Noise in Counter-Rotating Propfan Propulsion Systems

Rotor Interaction Noise in Counter-Rotating Propfan Propulsion Systems

Andreas Peters

Zoltán S. Spakovszky
e-mail: (zolti@mit.edu)

Department of Aeronautics and Astronautics,
Gas Turbine Laboratory,
Massachusetts Institute of Technology,
Cambridge, MA 02193

Due to their inherent noise challenge and potential for significant reductions in fuel burn, counter-rotating propfans (CRPs) are currently being investigated as potential alternatives to high-bypass turbofan engines. This paper introduces an integrated noise and performance assessment methodology for advanced propfan powered aircraft configurations. The approach is based on first principles and combines a coupled aircraft and propulsion system mission and performance analysis tool with 3D unsteady, full-wheel CRP computational fluid dynamics computations and aeroacoustic simulations. Special emphasis is put on computing CRP noise due to interaction tones. The method is capable of dealing with parametric studies and exploring noise reduction technologies. An aircraft performance, weight and balance, and mission analysis was first conducted on a candidate CRP powered aircraft configuration. Guided by data available in the literature, a detailed aerodynamic design of a pusher CRP was carried out. Full-wheel unsteady 3D Reynolds-averaged Navier-Stokes (RANS) simulations were then used to determine the time varying blade surface pressures and unsteady flow features necessary to define the acoustic source terms. A frequency domain approach based on Goldstein's formulation of the acoustic analogy for moving media and Hanson's single rotor noise method was extended to counter-rotating configurations. The far field noise predictions were compared to measured data of a similar CRP configuration and demonstrated good agreement between the computed and measured interaction tones. The underlying noise mechanisms have previously been described in literature but, to the authors' knowledge, this is the first time that the individual contributions of front-rotor wake interaction, aft-rotor upstream influence, hub-endwall secondary flows, and front-rotor tip-vortices to interaction tone noise are dissected and quantified. Based on this investigation, the CRP was redesigned for reduced noise incorporating a clipped rear-rotor and increased rotor-rotor spacing to reduce upstream influence, tip-vortex, and wake interaction effects. Maintaining the thrust and propulsive efficiency at takeoff conditions, the noise was calculated for both designs. At the interaction tone frequencies, the redesigned CRP demonstrated an average reduction of 7.25 dB in mean sound pressure level computed over the forward and aft polar angle arcs. On the engine/aircraft system level, the redesigned CRP demonstrated a reduction of 9.2 dB in effective perceived noise (EPNdB) and 8.6 EPNdB at the Federal Aviation Regulations (FAR) 36 flyover and sideline observer locations, respectively. The results suggest that advanced open rotor designs can possibly meet Stage 4 noise requirements. [DOI: 10.1115/1.4003223]

1 Introduction and Background

Advanced open rotor designs have the potential to extend the inherent fuel efficiency benefits of conventional turboprop engines to flight Mach numbers of up to 0.8. By recovering the residual swirl downstream of the front rotor, counter-rotating propfan (CRP) concepts can provide an increase of 6–8% in propulsive efficiency compared to single rotor configurations [1,2]. CRPs have been investigated intensively in the 1970s and 1980s and demonstrated significant reductions in fuel burn of up to 30% compared to high-bypass engines of 1980 vintage which are currently deployed on most civil aircraft [3]. Currently, propfans are being extensively studied again due to their potential for reduced environmental impact and their inherent noise challenge.

In order to explore the fuel burn benefits and acoustic performance of CRP aircraft configurations, a multidisciplinary integrated noise and performance assessment capability is required and presented in this paper. Existing methods are used for aircraft mission and engine cycle analysis, noise prediction of engine core and airframe sources, and for the aerodynamic propfan design and performance assessment.

A key aspect of the methodology is the capability to estimate the CRP noise. In previous work, various approaches have been undertaken to predict CRP noise and a summary can be found in Ref. [4]. Based on his helicoidal surface theory for propellers [5], Hanson developed one of the first analytical models for CRP noise prediction [6]. With the recent advances in numerical methods for aerodynamic and aeroacoustic analyses, hybrid methods based on coupling computational fluid dynamics (CFD) and computational aeroacoustics (CAA) have also been pursued [7–9]. However, CAA methods are expensive in CPU time and memory requirements due to the high mesh densities necessary to accurately resolve acoustic pressure disturbances. Thus, carrying out parametric studies in the CRP design phase using coupled CFD/CAA approaches is generally not yet feasible.

In the present paper, a frequency domain method for CRP noise is developed by extending Hanson's single rotor noise approach [10] to counter-rotating configurations. One of the main advantages is the low computation time requirement allowing the method to be used for detailed parametric studies and the investigation of advanced source noise mitigation concepts.

The theory requires the a priori determination of unsteady blade surface pressures to define the acoustic source terms. In the past, difficulties in obtaining the aerodynamic data have led to inaccurate noise results [10] but the emergence of CFD now provides the capability to estimate the unsteady blade loading. In this paper, high-fidelity full-wheel 3D RANS computations using the commercially available CFD tool NUMECA FINE/TURBO are demonstrated to successfully generate the required blade surface pressure information.

One of the primary concerns in developing a viable CRP engine design is the noise impact of open rotors, in terms of both in-flight cabin noise and takeoff/approach community noise. At cruise, thickness and loading noise are the key noise sources and the rotor-alone tones dominate the CRP spectrum. At the low-speed conditions, rotor-rotor interaction noise due to aerodynamic interference effects dominates the noise signature as described by Magliozzi et al. [11]. The main focus of the present work is on the computation of CRP interaction tones as they tend to control the radiated noise at the FAR 36 noise certification conditions.

It is assumed in this paper that the mechanisms responsible for the CRP interaction noise can be attributed to the following flow features: (1) rear-rotor upstream influence interacting with the front rotor, (2) tip-vortices shed from the front rotor interfering with the rear rotor, (3) front-rotor viscous wakes affecting the rear-rotor loading, and (4) front-rotor hub wake and hub boundary layer influencing the rear-rotor hub loading [12]. Several CRP noise reduction technologies such as variations in rotor-rotor spacing, rotor tip speed, or rotor blade count [13], as well as reductions in rear-rotor diameter [14] and blade wake management [15] have been explored in the past. In order to evaluate the effectiveness of these noise reduction technologies, the above noise source mechanisms are dissected and quantified for the takeoff condition using the newly developed CRP noise method.

The noise sources are dissected and the analysis serves as the basis for a redesigned CRP with the objective to reduce rotor-rotor interaction noise. For CRPs to be a viable alternative to advanced, high-bypass ratio, low-speed turbofan engine designs, their acoustic performance must be improved. The key question that arises is what noise reduction levels can possibly be achieved for an advanced open rotor design.

1.1 Scope of the Paper. The overall goal is to define an advanced CRP configuration with improved noise characteristics while maintaining the required aerodynamic performance for a given aircraft mission.[1] Working towards this aim, the objectives are to (1) dissect and quantify the impact of the mechanisms responsible for interaction tone noise, (2) explore and define necessary CRP noise reduction technologies, and (3) quantify the potential noise reductions on a consistent aircraft mission basis.

The conceptual framework is outlined first followed by a description of the aircraft configuration used to validate the methods and the definition of the baseline CRP aerodynamic design. The development of the CRP noise estimation method and the required CFD approach are then discussed and implemented for the baseline CRP. Next, the derived CRP noise method is validated by comparing the baseline CRP noise results to the measured data available for the same CRP configuration albeit with differences in the exact details of the blade profiles. Then, the noise sources are dissected and quantified. Based on this analysis, noise reduction technologies are devised and implemented in a redesigned CRP configuration. This design is again assessed for noise and the achieved interaction tone reductions are quantified. Finally, the acoustic benefits of advanced source noise mitigation concepts are investigated on the aircraft system level.

---

[1]Certification challenges such as blade containment are acknowledged but not taken into account in the present analysis.
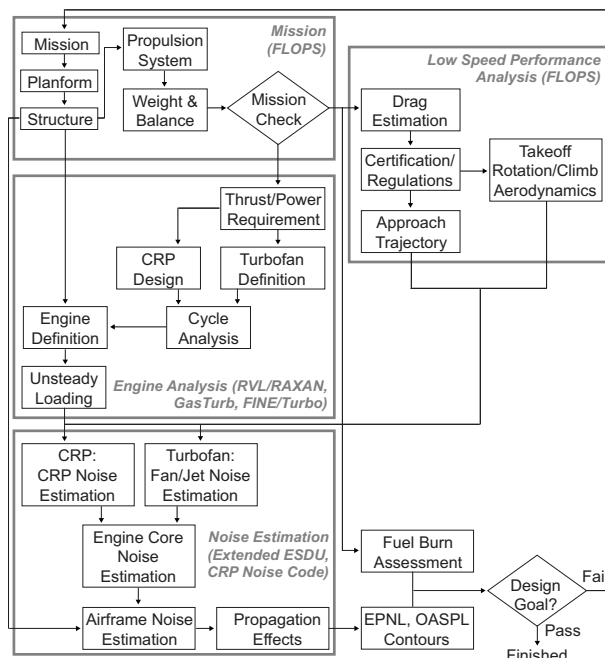
Fig. 1 Aerodynamic and acoustic performance assessment framework for counter-rotating propfans

2 Integrated Aircraft Performance and Noise Assessment Framework

An overview of the newly established integrated aircraft performance and noise assessment framework is depicted in Fig. 1. The overall methodology consists of four major modules and is capable of handling both turbofan and propfan powered aircraft configurations. In the following, a short description of the key modules is presented and more details are given in Ref. [16].

In the mission analysis module, the airframe, engine type, and engine/airframe integration parameters are specified. The component weights are calculated and a detailed mission performance analysis is performed using NASA's flight optimization software FLOPS [17]. The thrust requirement for the defined mission is input into the engine analysis module, which includes the cycle analysis for the specified turbofan or CRP gas generator using GASTURB [18]. In the case of a CRP powered aircraft, the aerodynamic design of the propfan is carried out using the single and dual rotor vortex-lattice methods, rotor vortex-lattice (RVL) and rotor axisymmetric analysis (RAXAN) [19]. In order to determine the time varying blade surface pressures required for the CRP acoustic analysis, full-wheel unsteady 3D RANS simulations of the counter-rotating stage are performed using NUMECA FINE/TURBO [20]. In the low-speed performance analysis module, the takeoff and approach trajectories are computed using a combination of a low-speed drag polar method [21] and the low-speed aerodynamics assessment method included in FLOPS. Iteratively, the engine/aircraft configuration characteristics required to meet the mission constraints are determined.

The airframe characteristics, engine cycle data, unsteady CRP blade loading, and takeoff and approach trajectories are then used in the noise estimation module. With the newly developed CRP noise estimation method and a combination of analytical and empirical methods (ESDU) [22], noise levels are computed for engine and airframe at the FAR 36 observer locations. The present paper focuses on the computation and assessment of interaction tone noise at takeoff conditions. The overall methodology is employed here to establish a credible baseline CRP design and to ensure that the assessment of an improved design is made on a consistent aircraft mission basis.

Table 1 Model scale baseline CRP characteristics and operating condition parameters (extracted from Ref. [23])

Configuration characteristics			Operating condition	
			Cruise	Takeoff
D_1 (m)	0.56	M	0.78	0.25
D_2 (m)	0.56	h (m)	10,670	Sea level
B_1	10	N_1 (rpm)	6,665	6,665
B_2	8	N_2(rpm)	6,665	6,665
x/D_1	0.224	β_1 (deg)	63.5	46.5
r_h/r_t	0.4	β_2 (deg)	63.5	46.5
φ_1 (deg)	40	J	3.90	1.43
φ_2 (deg)	40	C_T	1.10	1.18

Table 2 Computed model scale baseline CRP cruise performance compared to measured data

	Calculated	Measured (from Ref. [23])	Rel. error (%)
Front-rotor thrust coefficient at $C_{P,1}=2.32$	0.47	0.48	−2.1
Rear-rotor thrust coefficient at $C_{P,2}=2.61$	0.63	0.62	1.6

3 Aircraft Configuration and Propulsion System Design

A credible and representative baseline configuration is required to validate the performance and noise assessment methodology. An A320/B737 size, short to medium range twin-engine aircraft with advanced high-bypass turbofan engines was selected. The aircraft seats 150 passengers and has a range capability of 6,480 km (3,500 nm) at cruise Mach number 0.78 and initial cruise altitude capability of 10,670 m (35,000 ft). The takeoff field length requirement is constrained to 1980 m (6,500 ft). The baseline aircraft and datum turbofan engine characteristics with a by-pass ratio of 8.9 were defined in collaboration with industry.

Powered by two aft fuselage pylon mounted pusher CRPs, a propfan powered aircraft for the same mission was defined, denoted here as the baseline CRP configuration. The integration of the CRPs led to modifications of the turbofan powered baseline airframe. This included a rearward shift of the main wing and landing gear to meet static stability requirements and fuselage weight penalties due to structural reinforcements and cabin noise insulation. In addition, propfan blades, gearbox, and larger pylons resulted in a 31% propulsion system weight increase compared to the datum turbofan engine. More details on the aircraft configurations can be found in Ref. [16].

The development of the baseline CRP geometry was guided by data available in literature for a model scale CRP [23]. Selected configuration characteristics and cruise and takeoff operating condition details[2] are summarized in Table 1.

Assuming initial values for adiabatic efficiency, the overall stagnation temperature ratio distribution was first calculated based on the radial distribution of stagnation pressure ratio given in Ref. [23]. Assuming that additional mass flow is entrained through the rear rotor, the shaft work split between front and rear rotors was determined based on the given torque split.

Using the Euler turbine equation, the tangential velocity radial distributions for front and rear rotors were calculated. Imposing radial equilibrium and using a simplified actuator disk and control volume analysis, the static pressure radial distributions were computed and integrated to obtain front- and rear-rotor loading and thrust coefficients. The assumed values for adiabatic efficiency and entrained mass flow were iteratively varied until the exit swirl was minimized and the front- and rear-rotor performance agreed with the data in Ref. [23].

The analytically computed performance is summarized and compared to the measured data in Table 2. The front- and rear-rotor power coefficients $C_{P,1}$ and $C_{P,2}$ are determined from the measured shaft power and the known torque split of 45/55 given in Ref. [23]. For the operating condition analyzed, the calculated thrust results compare well with the measured performance.

Extracting the axial chord distribution and the stacking line location from Ref. [23] and assuming circular arc camber lines and a NACA 65A008 thickness distribution, the blade coordinates were defined guided by a velocity triangle analysis. Finally, the detailed aerodynamic design and performance investigation was carried out using the single and dual rotor vortex-lattice methods in RVL/RAXAN. However, the vortex-lattice approach does not capture compressibility effects. The analysis was performed at the takeoff condition defined in Table 1 and the detailed aerodynamic design was finalized by varying the blade angle settings and comparing the global performance with measurements summarized in Table 3.

For a takeoff blade setting of $\beta_1=\beta_2=46.5$ deg, the total power coefficient calculated with RVL/RAXAN is $C_P=2.79$, in good agreement with the measurements. The detailed blade geometry of the baseline CRP differs from that in Ref. [23] and consequently the takeoff aerodynamic performance is improved by $\Delta\eta_P=6.5\%$. The hub geometry is extracted from Ref. [23] and the baseline CRP is illustrated in Fig. 2.

The model scale CRP was sized to meet the thrust requirement at takeoff/top-of-climb by maintaining the tip Mach number and thrust coefficient and constraining the full scale CRP to equal tip speeds and diameters as in the model scale design. The resulting full scale baseline CRP characteristics and operating conditions at takeoff are summarized in Table 4.

The baseline CRP gas turbine cycle was based on the datum turbofan. The low-pressure turbine drives the propfan rotors through a gearbox with gear ratio of 8:1 in constant torque split design, similar to the gearbox featured in the 1989 PW/HS/Allison 578-DX propfan propulsion system with a gear ratio of 8.3:1 [24]. The selected gear ratio resulted in a high-speed low-pressure spool with $N_{LP,CRP}=7,872$ rpm. The datum turbofan low-pressure

Table 3 Model scale CRP performance at takeoff computed in RVL/RAXAN compared to data from Ref. [23]

	Calculated (RVL/RAXAN)	Measured (from Ref. [23])
C_P	2.79	2.78
C_T	1.31	1.18
η_P	67.1	60.6

Fig. 2 Baseline CRP design

---

[2]Advance ratio, power coefficient, and thrust coefficient are defined using the average shaft speed $N=(N_1+N_2)/2$ and average rotor diameter $D=(D_1+D_2)/2$.
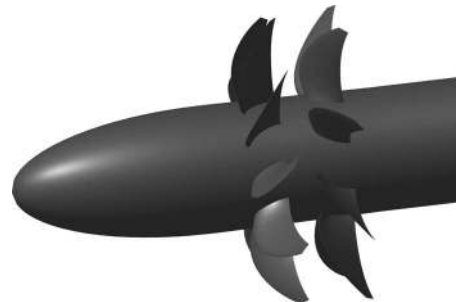
Table 4 Full scale baseline CRP configuration and takeoff operating condition parameters

Configuration characteristics		Takeoff operating condition	
D_1 (m)	3.81	M	0.25
D_2 (m)	3.81	h (m)	Sea level
B_1	10	N_1 (rpm)	934
B_2	8	N_2 (rpm)	934
x/D_1	0.224	β_1 (deg)	46.5
r_h/r_t	0.4	β_2 (deg)	46.5
φ_1 (deg)	40	J	1.43
φ_2 (deg)	40	C_T	1.31
		η_P (%)	67.1

spool operates at $N_{LP,fan}=3,800$ rpm; thus, a reduction in engine core size was required for the baseline CRP configuration. Further details of this design can be found in Ref. [16].

4 CRP Noise Estimation Method

The CRP noise estimation method is based on Goldstein's formulation of the acoustic analogy for moving media [25] and Hanson's frequency domain single rotor noise method [10]. Thickness and loading noise sources are the main sources implemented in the CRP noise estimation method. For thin blades, significant quadrupole noise radiation is a strictly transonic phenomenon as, for example, reported by Hanson and Fink [26]. The CRP blade designs investigated in this work are highly swept and relative tip Mach numbers are below the critical value of 0.85 at the low-speed conditions considered here for noise assessment. Therefore, quadrupole sources are currently not accounted for but can be included for cruise noise calculations in the future. In the following, the extension of Hanson's single rotor noise method to counter-rotating configurations is briefly outlined.

The Ffowcs–Williams and Hawkings acoustic analogy formulation generalized for a moving medium can be written as

$$p'(\mathbf{x},t) = -\int_{-T}^{T}\int_{A(\tau)} \rho_0 V_N \frac{DG}{D\tau} dA(\mathbf{y})d\tau + \int_{-T}^{T}\int_{A(\tau)} F_i \frac{\partial G}{\partial \tau} dA(\mathbf{y})d\tau \tag{1}$$

where $p'(\mathbf{x},t)$ is the acoustic pressure disturbance at observer location $\mathbf{x}=(x,y,z)^T$ and time t.

The thickness noise source is described by the first term in Eq. (1). V_N denotes the normal surface velocity and $V_N dA d\tau$ is the volume displaced by the surface element dA in the time increment $d\tau$. G is a Green's function and $D/D\tau$ is the convective derivative. The loading noise source is given by the second term in Eq. (1) where $F=(F_r, F_\Phi, F_{x'})^T$ and $F_i dA$ denotes the force on blade surface element dA in direction i.

As described in Ref. [10], thickness and loading noise can be calculated independently. Representing the time signal $p'(\mathbf{x},t)$ as a Fourier series, the single rotor thickness noise harmonic P_{Tm} for blade passing frequency harmonic m at observer location $\mathbf{x}$ can be expressed as

$$P_{Tm}(\mathbf{x}) = \gamma B \int_A e^{-imB\varphi_S} \frac{1}{2\pi} \int_0^{2\pi} M_N \left(M \frac{\partial G_m}{\partial x_0} - ik_m G_m \right)$$
$$\times e^{-imB\varphi_0} d\varphi_0 dA \tag{2}$$

where $M_N = V_N/c_0$ is the Mach number normal to the blade surface, $k_m = mBM_t$ is the wavenumber, and $M_t = \Omega r_t/c_0$ is the tip Mach number. B denotes the number of blades. The axial and tangential source coordinates are given by x_0 and Φ_S, respectively, and the Green's function is

$$G_m = \frac{e^{ik_m\sigma}}{4\pi S} \tag{3}$$

with the phase radius σ given by

$$\sigma = \frac{M(x-x_0)+S}{1-M^2} \tag{4}$$

and the amplitude radius S written as

$$S = \sqrt{(x-x_0)^2 + (1-M^2)((y-y_0)^2 + (z-z_0)^2)} \tag{5}$$

Analogous to the thickness noise calculation, the single rotor loading noise harmonic P_{Lm} can be written as

$$P_{Lm}(\mathbf{x}) = B \int_A e^{-imB\varphi_S} \frac{1}{2\pi} \int_0^{2\pi} F_i(\varphi_0 - \varphi_S) \frac{\partial G_m}{\partial y_i} e^{-imB\varphi_0} d\varphi_0 dA \tag{6}$$

where the elements of the blade loading $F_i dA$ are computed using 3D unsteady RANS simulations and the Green's function derivatives are calculated analytically.

4.1 Extensions to Counter-Rotating Propfans. The unsteady interaction of the two rotors due to wake, tip-vortex, and potential field effects is captured in the aerodynamic calculations. Since the acoustic analogy is based on the coupled aerodynamics, the acoustic interaction is inherently accounted for by carefully superposing the noise fields from the two rotors as suggested by Hanson [6].

Thickness noise is produced at multiples of the blade passing frequency only such that the harmonic order m takes on all integer values from 1 to $+\infty$. In order to account for the CRP inherent interaction tones caused by unsteady blade loading, the formulation for single rotor loading noise in Eq. (6) has to be modified. For the general case of unequal tip speeds and blade counts, the observer will perceive frequencies at

$$f = nBPF_1 + k(BPF_2 - BPF_1) \tag{7}$$

where $n=1,2,\ldots,\infty$, $k=0,1,\ldots,n$, and $BPF_{1,2}=B_{1,2}N_{1,2}$ denotes the blade passing frequency of the respective rotor. The value of the sound harmonic m in Eq. (6) is changed to $m'=f/BPF$, where $BPF=BPF_1$ or $BPF=BPF_2$, depending on which rotor loading noise is computed. In contrary to the single rotor case in which each blade experiences identical loading changes and thus generates identical noise signals, it is important to note that in the general case of unequal tip speeds and blade counts, or in the presence of an upstream pylon or angle of attack effects, the individual rotor blades do not necessarily emit identical noise signals. Thus, instead of simply multiplying the source term by the blade number B in Eq. (6), the noise signals from each blade b have to be added up while taking into account the phase lags due to the blade position. Implementing these modifications, Eq. (6) becomes

$$P_{Lm,CRP}(\mathbf{x}) = \sum_{b=1}^{B} e^{-im'B\varphi_{ref}(b)} \int_A e^{-im'B\varphi_S} \frac{1}{2\pi}$$
$$\times \int_0^{2\pi} F_{b,i} \frac{\partial G_{m'}}{\partial y_i} e^{-im'B\varphi_0} d\varphi_0 dA \tag{8}$$

where the reference angle accounting for the blade position is given by

$$\varphi_{ref}(b) = (b-1)\frac{2\pi}{B} \tag{9}$$

In Eq. (8), $F_{b,i}$ denotes the force per unit area on the surface of blade b in direction i (radial, tangential, and axial).

A conceptual outline of the established CRP noise estimation method is depicted in Fig. 3. Required inputs are the blade geom-
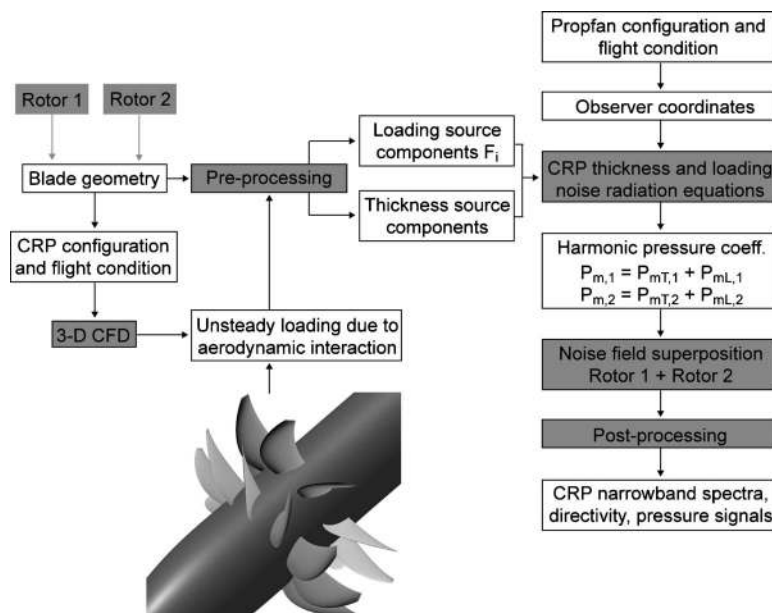
Fig. 3   CRP noise estimation methodology

etries of the two rotors, the CRP configuration details (such as, for example, rotor-rotor axial spacing), operating condition parameters, and the observer coordinates relative to the CRP. Using the unsteady blade loading data calculated externally (for example, 3D CFD), the thickness and loading source components are computed. In order to obtain the full CRP noise spectrum, the formulations for thickness and loading noise in Eqs. (2) and (8) are evaluated separately for each rotor. The noise fields are then superposed to determine the CRP narrowband spectrum or acoustic pressure signals.

5   CFD Simulation Setup

3D unsteady RANS simulations were carried out using the commercially available software package NUMECA FINE/TURBO to investigate the aerodynamic interaction between the two rotors and to obtain the time varying blade pressures. Similar to previous studies [7,9], the eddy viscosity is resolved using the one-equation Spalart–Allmaras turbulence model [27]. Multiblock structured hexahedral grids were used for the baseline and advanced design CRPs. To accurately resolve the front-rotor viscous wakes and

tip-vortices, the meshes between the two rotors and around the blade tips were generated with particular care. The blade grid topology (O4H) was extended all the way to the far field boundary to assure a continuous grid and to eliminate all nonmatching block patches at the interface between the rotor passage and far field subdomains. At the interface between the two rotor relative frames, the radial node distribution is continuous. The governing equations are solved in the relative frame leading to high relative Mach numbers near the far field radial boundary. This in turn can induce excessive artificial dissipation leading to nonphysical rotational flow in the far field regions. To avoid this, the far field radial boundary was located at $4D_1$, far enough from the CRP domain to avoid interference with the capture streamtubes.

The grid-block topology of the baseline CRP single passage grid generated using NUMECA'S AUTOGRID 5 is depicted in Fig. 4. There are 101 radial grid points in the rotor passage, 85 grid points in the pitchwise direction across the passage, and 121 grid points on the blade suction and pressure surfaces in the chordwise direction. All of the unsteady simulations used to obtain the time-dependent blade loading for the CRP noise calculations were car-
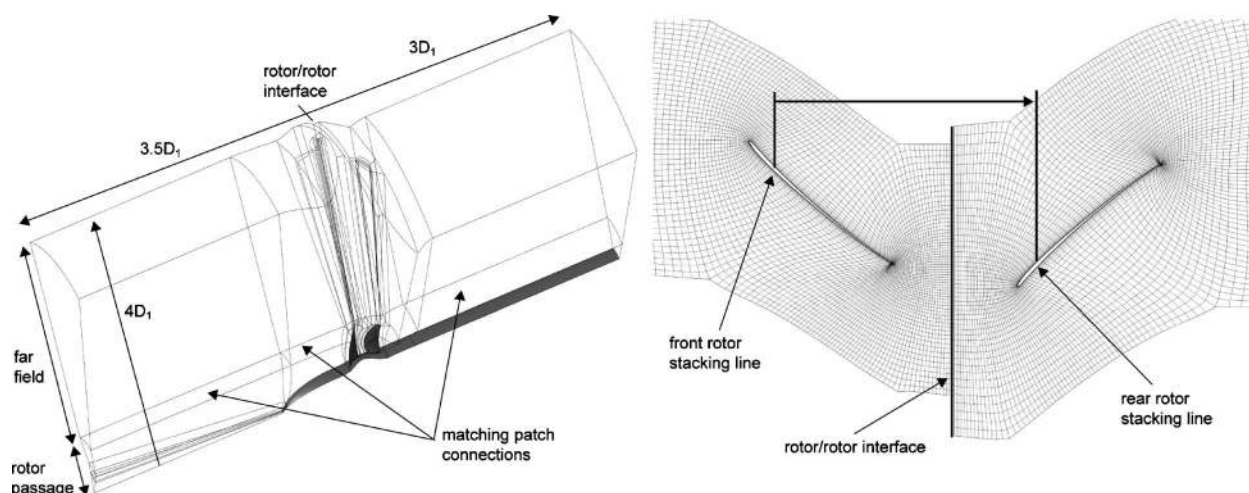

Fig. 4   Baseline CRP grid-block topology (left) and close-up of rotor meshes at midspan (right)
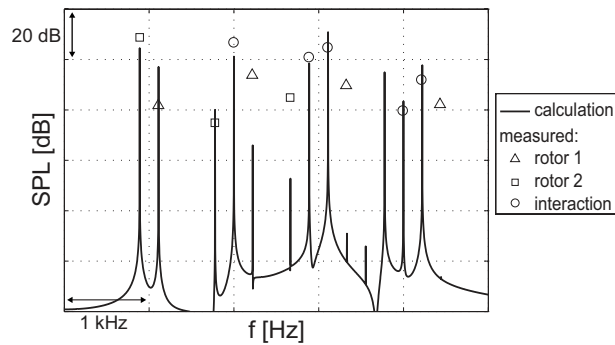
Fig. 5 Baseline CRP spectrum at 85 deg polar angle from the inlet centerline

ried out as full-wheel computations featuring 16.5 million cells for the baseline CRP.

In addition to the investigation of different grid topologies, detailed grid convergence studies were conducted by applying FINE/TURBO's multigrid technique and by gradually increasing the grid density between the two rotors and on the blade surfaces. Steady and unsteady blade pressure results as well as wake and tip-vortex resolution were used to determine when grid convergence was reached. The effect of time step size on the unsteady flow solution was studied as well. In general, about 50,000 iterations were required to reach a settled unsteady flow solution. More details on the grid and time step studies can be found in Ref. [16].

The time varying pressure data obtained from the CFD calculations is Fourier transformed to determine the loading harmonics required as inputs to the CRP noise estimation method. In the absence of angular inflow or upstream pylon effects, the rear-rotor upstream influence causes the loading on the front rotor to vary at frequencies

$$f_{\text{load},1} = kBPF_2\left(1 + \frac{N_1}{N_2}\right) \tag{10}$$

where the loading harmonic $k = 0, 1, 2, \ldots, \infty$. Similarly, the front-rotor viscous wakes and tip-vortices lead to rear-rotor unsteady loading effects at frequencies

$$f_{\text{load},2} = kBPF_1\left(1 + \frac{N_2}{N_1}\right) \tag{11}$$

With the above, the loading waveform is reconstructed as part of the preprocessing in the CRP noise estimation method to determine the loading source components $F_{b,i}$ in the CRP loading noise calculation described in Eq. (8).

6 CRP Noise Method Validation

In order to validate the CRP noise estimation method, computed baseline CRP noise results are compared to acoustic mea-

surement data provided by the industry sponsor for the same CRP configuration (operating conditions and overall geometry such as hub-to-tip ratio, rotor-rotor axial spacing, and sweep were identical). However, it is important to note that the details of the blade geometry (camber, thickness, or stacking line distribution) were not available from the literature and are not necessarily the same. In addition, the measurements included a pylon upstream of the CRP whereas uniform inflow was assumed in the computed baseline CRP noise results.

For an axial microphone position with polar angle $\theta = 85$ deg, the narrowband spectrum is given in Fig. 5. In general, the first six interaction tones at frequencies $BPF_1 + BPF_2$, $BPF_1 + 2 \times BPF_2$, $2 \times BPF_1 + BPF_2$, $BPF_1 + 3 \times BPF_2$, $3 \times BPF_1 + BPF_2$, and $2 \times BPF_1 + 2 \times BPF_2$ are in good agreement with the measured data marked by the circles. The measured rotor-alone tones (triangles and squares) are strongly influenced by the upstream pylon present in the experiments and therefore show some discrepancies compared to the calculated results, particularly, for higher harmonics.

Polar directivity results are depicted on the left in Fig. 6 for the first interaction tone at frequency $BPF_1 + BPF_2$. The front-rotor contribution to the interaction tone level is marked by the dashed grey line and the contribution from the rear rotor is marked by the grey line with diamond symbols. The acoustic measurement data is indicated by the circles and the total computed noise is marked by the black line.

The interaction tone noise levels at frequencies $2 \times BPF_1 + BPF_2$ and $BPF_1 + 2 \times BPF_2$ are shown in the center and right-hand plot of Fig. 8, respectively. Overall, there is good agreement between the calculated and measured data. The larger discrepancies at around $\theta = 75$ deg of the $BPF_1 + BPF_2$ interaction tone and at the low polar angle range of the $2 \times BPF_1 + BPF_2$ interaction tone were later explained to be due to (1) slight differences in blade geometry between the baseline CRP and the experimentally tested model CRP, yielding differences in the aerodynamic features that govern the interaction tone noise, and (2) to a lesser degree the significant influence of nonuniform inflow generated by the upstream pylon as investigated in detail, for example, by Janardan and Gliebe [13] and Woodward [28].

7 Baseline CRP Acoustic Assessment

Before investigating the interaction tone noise levels in detail, the underlying mechanisms are briefly outlined. The results of the baseline CRP acoustic assessment are discussed next, followed by the description of the CRP redesign for reduced interaction noise and the comparison of the baseline and advanced CRP acoustic and aerodynamic performance results.

7.1 Interaction Tone Noise—Source Mechanisms. The aerodynamic mechanisms producing the CRP interaction noise can be categorized into the four effects described earlier: rear-rotor upstream influence interacting with the front rotor, front-rotor tip-vortices interfering with the rear rotor, front-rotor viscous
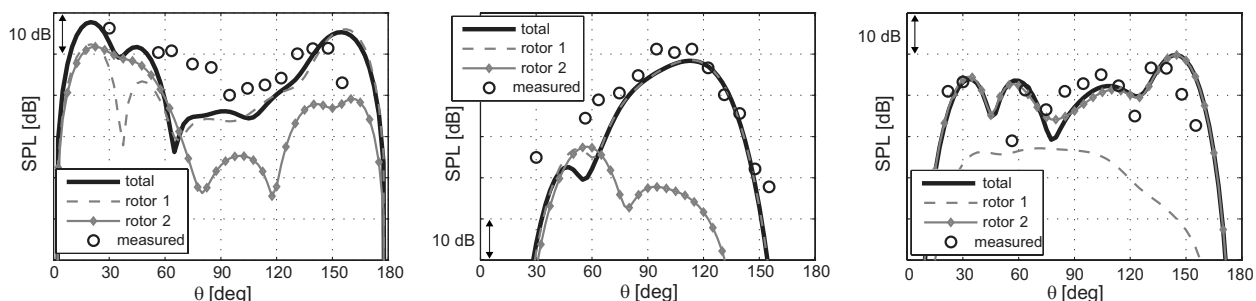

Fig. 6 Baseline CRP interaction tone noise level at frequency $BPF_1 + BPF_2$ (left), at $2 \times BPF_1 + BPF_2$ (center), and at $BPF_1 + 2 \times BPF_2$ (right)
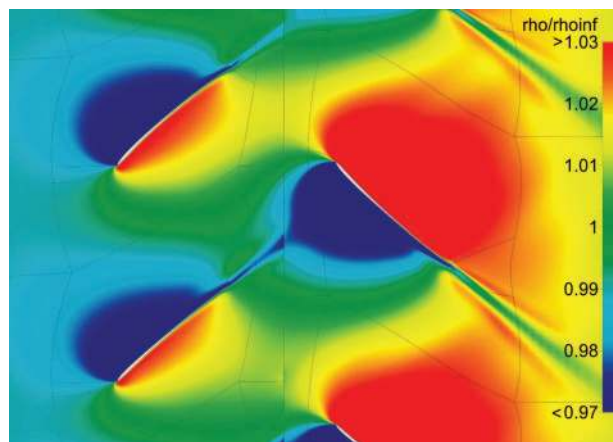
Fig. 7 Baseline CRP density distribution at midspan

Fig. 9 Baseline CRP entropy distribution near hub (at 10% span)

wakes interacting with the rear rotor, and front-rotor hub wake and hub boundary layer affecting the rear-rotor hub loading. The results given in the following are for takeoff conditions at $M = 0.25$.

The rear-rotor potential field directly influences the front-rotor loading and the flow field around the CRP blades for a radial cut at midspan is shown in Fig. 7. The baseline CRP is operated at equal tip speeds such that a front-rotor blade interacts $2B_2 = 16$ times with the potential field of a rear-rotor blade during one revolution.

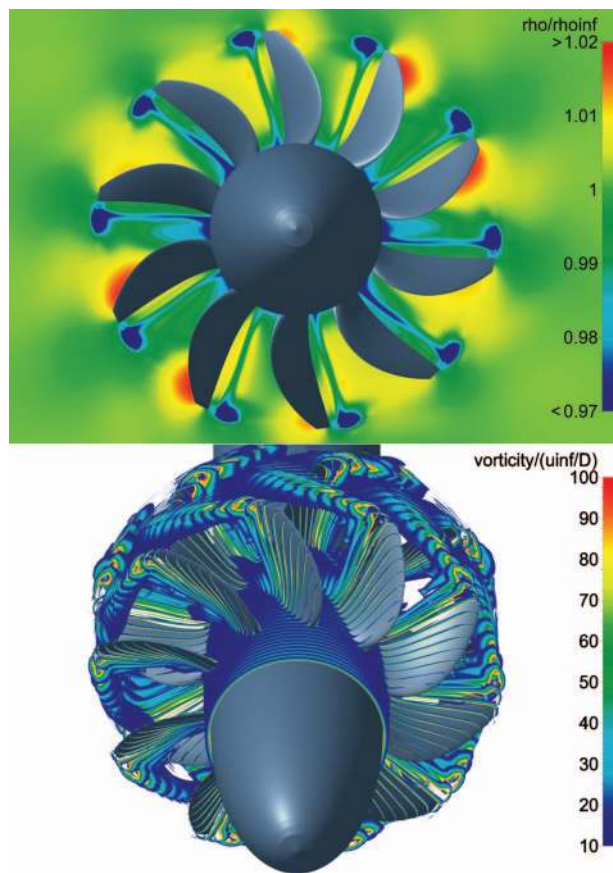The second noise source mechanism investigated is the interac-

Fig. 8 Baseline CRP density distribution at $x/D_1 = 0.12$ (top) and blade-tip vortex system (bottom): front-rotor tip-vortices interact with rear rotor
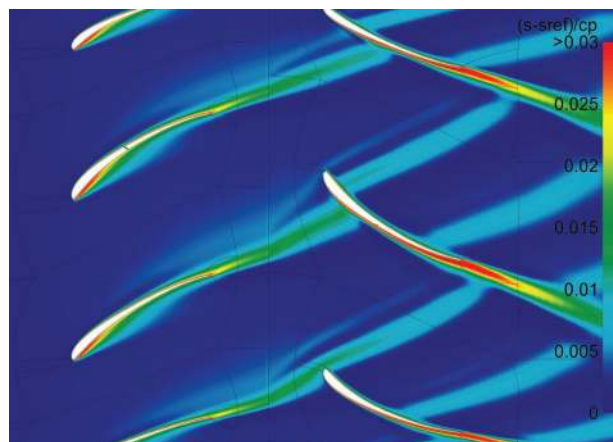
tion of the front-rotor tip-vortices, represented as low density regions on the top in Fig. 8. The vortex system is also shown on the bottom highlighting the helical motion and convection of the tip-vortices through the interface between the front- and rear-rotor reference frames and interacting with the rear rotor.

The interactions of the front-rotor wakes and the hub wake and endwall boundary layer with the rear rotor represent the third and fourth noise source mechanisms, respectively. The viscous wakes are depicted in Fig. 9 near the hub at 10% span. Similar to the tip-vortex noise source mechanism, a rear-rotor blade interferes $2B_1 = 20$ times with the viscous wake during one rotor revolution. The thin secondary wake preceding the blade wake observed in Fig. 9 is due the flow separation and reattachment on the blade suction surface near the leading edge of the highly cambered hub profile.

7.2 Dissection of Interaction Tone Noise. Next, the underlying noise source mechanisms are dissected and their contributions to the interaction tone noise levels are quantified. For example, in order to quantify the relative effect of tip-vortex interaction at the interaction tone frequency under consideration, the loading source is computed between 75% and 100% on the rear rotor only. In this spanwise range, which was determined by investigating the tip-vortex trajectory, it is hypothesized that the tip-vortex interaction mechanism is the dominant contributor to the interaction tone noise. Similarly, the hub wake/endwall boundary layer noise source mechanism is assumed to control the interaction noise generation in the range of 0–12.5% span, and the viscous wake related mechanism is conjectured to be the dominant contributor in the remaining spanwise range. The influence of the rear-rotor potential field is calculated by accounting for the loading sources on the front rotor only. The noise source dissection approach is summarized in Table 5 below.

The relative contributions of each of these mechanisms are depicted in Fig. 10 by means of interaction tone directivities at frequencies $BPF_1 + BPF_2$, $2 \times BPF_1 + BPF_2$, and $BPF_1 + 2 \times BPF_2$, respectively.

For the first interaction tone, the noise level is dominated by a

Table 5 Approach to dissecting baseline CRP interaction noise source mechanisms

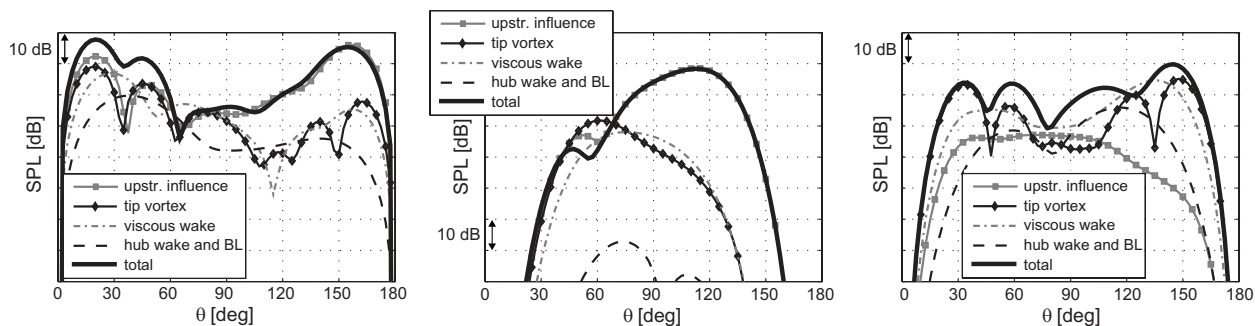| Noise source mechanism	Contributing rotor	Spanwise range
Upstream influence	Front	0–100%
Tip vortex	Rear	75–100%
Viscous wake	Rear	12.5–75%
Hub wake/endwall BL	Rear	0–12.5%

Fig. 10 Dissection of CRP noise mechanisms for interaction tones BPF_1+BPF_2 (left), $2\times BPF_1+BPF_2$ (center), and $BPF_1+2\times BPF_2$ (right), baseline CRP, $M=0.25$

combination of upstream influence, tip-vortex, and viscous wakes in the forward arc. Investigation of the unsteady flow field showed that the pressure fluctuations on the pressure side of the front rotor caused by the rear-rotor potential field are significantly larger than those of the rear rotor stemming from the influence of front-rotor viscous wakes and tip-vortices.[3] The generated noise is radiated rearward and the differences between the magnitudes of the fluctuations resulted in the rear-rotor upstream influence dominating the noise level in the aft arc at the first interaction tone frequency.

It should be noted that destructive and constructive interference effects can lead to the total CRP noise level falling below the contributions from either the front or the rear rotor as observed, for example, for the polar angle range between 60 deg and 80 deg for the first interaction tone on the left in Fig. 10.

Tip-vortex interaction is suggested to control the interaction tone $2\times BPF_1+BPF_2$ up to a polar angle of 70 deg. In the aft arc, the potential field interaction dominates as shown in the center plot of Fig. 10. Over a wide range of polar angles, the interaction tone $BPF_1+2\times BPF_2$ is again governed by all noise source mechanisms as shown on the right in Fig. 10.

The noise source dissection analysis for the first six interaction tones is summarized in Fig. 11. Mean sound pressure levels (SPLs) were computed for the forward and aft arcs, respectively, and the noise source mechanisms were quantified based on their acoustic pressure contributions to the mean sound pressure levels. In conjunction with the detailed directivity results, this approach allows to directly assess and to prioritize the impact of the different noise source mechanisms. The following observations can be made. (1) As expected, the interaction of rear-rotor upstream influence with the front rotor dominates the interaction tones at multiple frequencies of the front rotor, $2\times BPF_1+BPF_2$, and $3\times BPF_1+BPF_2$. (2) Similarly, noise from tip-vortex interaction with the rear rotor is more pronounced in interaction tones at multiple frequencies of the rear rotor, $BPF_1+2\times BPF_2$, and $BPF_1+3\times BPF_2$. (3) Interaction tones at equal multiples of rotor frequency, BPF_1+BPF_2 and $2\times BPF_1+2\times BPF_2$, are suggested to be governed by all noise source mechanisms.

It is important to note the following implication relative to potential noise reduction strategies; although certain interaction tones are dominated by one or another mechanism with possible preferences either in the front or rear arcs, to achieve significant interaction tone noise reductions, *all noise mechanisms* need to be addressed. This is the key objective of the advanced design CRP discussed next.

8 Advanced CRP Design For Low Noise

Based on the above baseline CRP acoustic investigation, the CRP was redesigned with the focus on reducing the interaction

tone noise while maintaining or possibly improving the aerodynamic performance. The following four noise reduction technologies were implemented: (1) increased rotor-rotor axial spacing, (2) reduction of the rear-rotor diameter, (3) differential tip speeds, and (4) blade count variations.

Increasing the axial spacing between the rotor results in an increased decay of the front-rotor viscous wakes and tip-vortices before they interact with the rear rotor. In addition, the strength of the rear-rotor potential field near the front rotor is significantly reduced. Therefore, it is hypothesized that increased rotor-rotor spacing will mitigate several interaction tone mechanisms, in agreement with noise reductions previously reported by, for example, Janardan and Gliebe [13] and by Woodward and Gordon [14].

The rear-rotor diameter was also reduced to potentially eliminate the interaction of the front-rotor tip-vortex [12]. The rear rotor was clipped at 75% span based on a tip-vortex trajectory analysis. For a reduced rear-rotor diameter, the blade loading needs to be increased to maintain the thrust level. This can be achieved either by increasing the blade angle setting or the tip speed, or a combination thereof. In return, however, a higher rear-rotor blade loading leads to an increased upstream influence, which can impair the acoustic benefits of increased rotor-rotor axial spacing. Compared to the baseline CRP design, the thrust level was maintained at the takeoff condition, which is relevant for the noise assessment. In order to limit the loading increase on the rear rotor while maintaining thrust, the number of blades was increased from 8 to 11. A model scale version of the advanced design CRP configuration is used for the acoustic assessment and dissection of noise mechanisms such that the results can be compared to the model scale baseline CRP data on a consistent basis.

Similar to the baseline CRP, the advanced design CRP was also sized to full scale at the takeoff condition. Both designs feature the same front-rotor diameter and tip speed but the rear-rotor characteristics differ as summarized in Tables 4 and 6. Simulating the full scale advanced design CRP in RVL/RAXAN, it was ensured
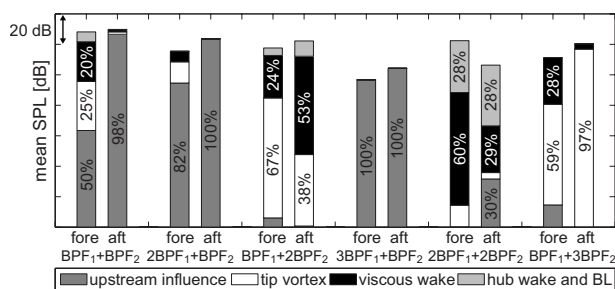

Fig. 11 Baseline CRP noise mechanism contributors to first six interaction tones (percentages based on p'^2 averaged over forward and aft polar arcs), $M=0.25$

Table 6 Full scale advanced design CRP configuration and takeoff operating condition parameters

Configuration characteristics		Takeoff operating condition	
D_1 (m)	3.81	M	0.25
D_2 (m)	3.24	h (m)	Sea level
B_1	10	J	1.79
B_2	11	N_1 (rpm)	934
x/D_1	0.35	N_2 (rpm)	747.2
r_h/r_t	0.4	β_1 (deg)	50.3
		β_2 (deg)	50.5
		η_P (%)	67.1

Fig. 14 Advanced design CRP noise mechanism contributors to first six interaction tones (percentages based on p'^2 averaged over forward and aft polar arcs), $M=0.25$

that the thrust level was maintained. The advanced CRP is the result of a first design iteration with the objective to reduce noise. A second design iteration is needed to assess cruise performance and fuel burn levels which could not be carried out due to time constraints.

Since the rear-rotor tip speed was reduced for the advanced design CRP, the required planetary gearbox ratio between the low-pressure spool and the rear-rotor shaft increased from 8:1 to 10.1:1. Compared to the baseline CRP, the loading on the front-rotor blades is larger than the rear-rotor load, which is reflected in a reversal of the torque split. The larger torque is transferred through the planetary gearbox carrier. As the carrier driven rotor must be located farthest away from the engine core, the advanced CRP design is suggested to be more suitable for a tractor configuration. A 5% increase in the propulsion system weight was assumed in the mission and overall performance analysis to account for the increased rotor-rotor spacing and the additional blades. More details can be found in Ref. [16].
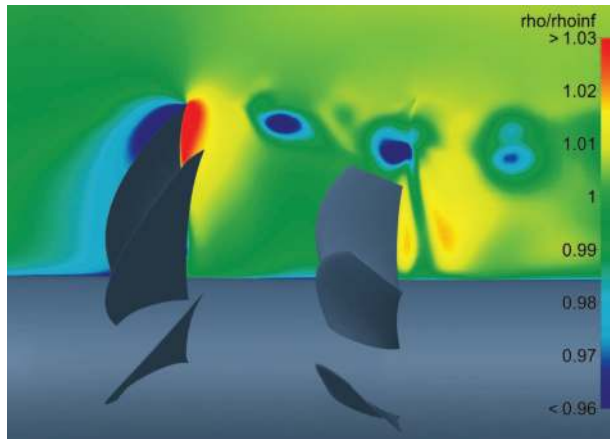

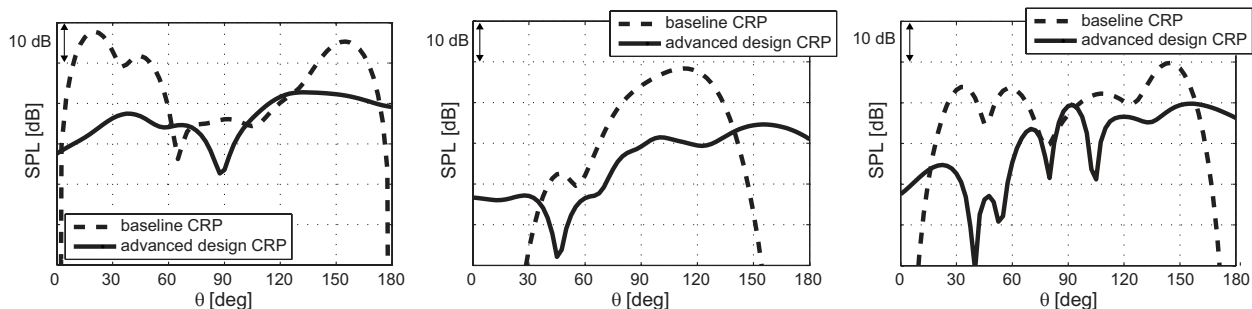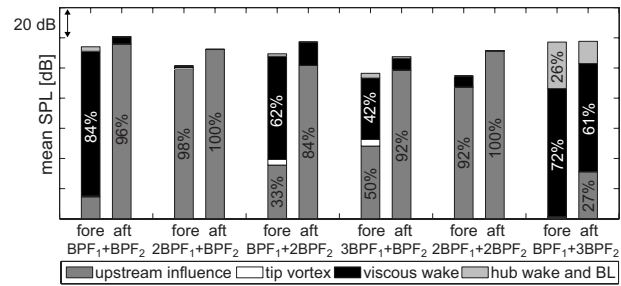**Fig. 12 Advanced design CRP geometry and near-field density distribution**

The CFD simulations necessary for further aerodynamic and acoustic analysis of the advanced CRP design required the generation of a modified full-wheel mesh. Compared to the baseline CRP grid, additional cells were needed in the blocks between the two rotors as the rotor-rotor axial spacing increased. Moreover, clipping the rear rotor required an increase in grid density between the rear-rotor blade tip and the far field subdomain to accurately resolve the front-rotor tip-vortex in this region. Consequently, the advanced design CRP full-wheel mesh was comprised of 26 million cells. The geometry of the advanced design CRP is presented in Fig. 12 along with the near-field density distribution showing the front- and rear-rotor tip-vortices as well as the rear-rotor viscous wake.

8.1 Acoustic Performance for Advanced Design CRP. For the advanced design CRP, the periodicity is $4T_2=5T_1$, as the tip speed ratio is $N_1/N_2=1.25$. Therefore, in order to capture all of the loading frequencies, it is necessary to record the surface pressure for every blade over four rear-rotor revolutions (equivalent to five front-rotor revolutions). Due to data processing and CPU time limitations, the remaining analysis is based on surface pressures recorded for 1.5 rear-rotor revolutions after reaching the quasi-periodic flow conditions.

The first three interaction tone directivities for the baseline and advanced design CRPs are compared in Fig. 13. For all three interaction tone frequencies, the noise levels are significantly reduced over a wide range of polar directivity angles. The advanced design CRP interaction tone levels do not approach zero at low and high polar angles which is conjectured to be due to the influence of unequal tip speeds. For equal tip speeds, there are substantial destructive superposition effects strongly reducing the noise levels close to the axis of rotation.

The dissected CRP noise mechanisms are presented in Fig. 14. Similar to the baseline CRP case, the effects of the noise mechanisms are quantified by computing the loading source terms for a spanwise section only. Based on analyzing the tip-vortex trajectory, it is assumed that the acoustic interaction of the front-rotor
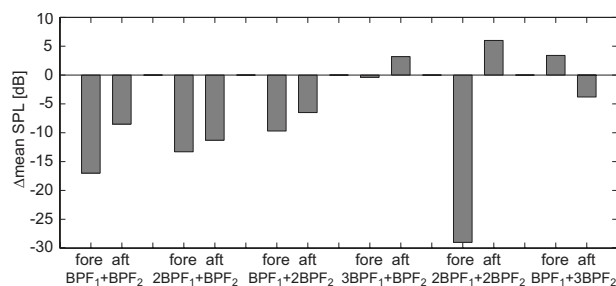

Fig. 13 Comparison of baseline and advanced design CRP directivity at interaction tone frequencies BPF_1+BPF_2 (left), $2\times BPF_1+BPF_2$ (center), and $BPF_1+2\times BPF_2$ (right), $M=0.25$

Fig. 15 Relative change in mean SPL for advanced design CRP compared to baseline CRP

Table 8 Total EPNL in EPNDB at FAR 36 sideline location

	Datum turbofan aircraft	Baseline CRP aircraft	Advanced design CRP aircraft
Estimated	89.7	94.1	85.5
Stage 4	96.6	96.8	96.8

tip-vortex with the rear-rotor blade tip is limited to 90–100% of rear-rotor span. The front-rotor viscous wakes affect the rear rotor over the 17–90% rear-rotor span range, while the front-rotor hub wake influences the rear-rotor loading between 0% and 17% span.

As expected, clipping the rear-rotor blade results in a significant reduction in tip-vortex interaction, as depicted in Fig. 14. Viscous wake and upstream influence effects are the dominating noise source mechanisms as both the wake strength and the strength of the potential field interactions are substantially increased due to a higher front-rotor loading.

Overall, the noise levels are greatly reduced, in particular, for the first three interaction tones, as summarized in Fig. 15. Averaged over all interaction tones investigated, the mean SPL is reduced by 7.25 dB, for the first three interaction tones, the average reduction is 11 dB. In contrast to the baseline CRP where interaction tone levels approach zero at low and high polar angles, the interaction tone levels of the advanced design CRP are spread over a larger range of polar angles. This effect actually leads to an increase in mean SPL for some of the higher interaction tone frequencies, such as, for example, in the forward arc of interaction tone at $BPF_1 + 3 \times BPF_2$.

In summary, the acoustic performance investigations of the baseline and advanced design indicate that, in order to achieve significant noise reductions, it is important to implement noise reduction technologies that address *all* noise source mechanisms at play as the overall noise is governed by a multiple sources of similar strength. Clipping the rear rotor, increasing the axial spacing, and operating at differential tip speeds are effective approaches to reduce CRP interaction noise. Further increasing the axial spacing is assumed to result in additional acoustic benefits. However, the trade-offs between acoustic and aerodynamic performance need to be carefully investigated as larger rotor-rotor spacings can increase the propulsion system weight and reduce the amount of swirl recovered by the rear rotor.

9 System Level Noise Assessment

Using the overall integrated performance and noise assessment methodology depicted in Fig. 1, the acoustic performance of the baseline and advanced design CRP aircraft arrangements was investigated. For the analysis of the CRP aircraft configurations, CRP, low-pressure compressor, combustor, low-pressure turbine, and airframe noise sources are accounted for. In the case of the turbofan powered aircraft, fan and jet noise are additionally included in the assessment.

Table 7 Total EPNL in EPNDB at FAR 36 flyover location

	Datum turbofan aircraft	Baseline CRP aircraft	Advanced design CRP aircraft
Estimated	87.6	94.2	85.0
Stage 4	91.2	91.5	91.5

Pylon and angle-of-attack effects were not included in the CFD analysis and any aerodynamic interaction of nonuniform inflow with the CRP rotors is not captured. The presence of an upstream pylon or angle-of-attack effects leads to unsteady blade loading at the BPF harmonics which in turn influences the rotor-alone tone noise. As a result, the rotor-alone tones are underestimated in the present analysis. However, the interaction tones generally dominate the CRP noise spectra at low-speed conditions [11]. Thus, underestimating rotor-alone noise is not believed to significantly affect overall CRP noise levels. In addition, the analysis presented here is at FAR 36 flyover and sideline observer locations only. The computed effective perceived noise level (EPNL) values at the FAR 36 flyover observer location are tabulated for the three investigated aircraft configurations in Table 7 along with the Stage 4 noise limits.[4] CRP noise was found to be the dominant noise source in both the baseline CRP and advanced design CRP configurations. By implementing advanced source mitigation concepts, the CRP noise was significantly reduced. Since the noise from the remaining engine sources is substantially decreased due to the reduction in core size, the total noise generated by the advanced design CRP powered aircraft was reduced relative to the datum turbofan configuration. Relative to the baseline CRP aircraft arrangement, a total noise reduction of 9.2 EPNdB is suggested by implementing noise reduction technologies.

Overall, the results suggest that the baseline CRP powered aircraft does not reach the Stage 4 noise limits by a considerable margin (2.7 EPNdB). On the other hand, the advanced design CRP was found to meet the Stage 4 noise restriction with a margin of 6.5 EPNdB. A noise breakdown for the different engine and airframe sources together with details on the system level noise assessment can be found in Ref. [16].

At the FAR 36 sideline location, the implementation of advanced source mitigation concepts led to a total noise level reduction of 8.6 EPNdB, as tabulated in Table 8. Keeping in mind the aforementioned assumptions, the results suggest that Stage 4 noise limits can be met by all three configurations investigated. The margin is smallest for the baseline CRP aircraft (2.7 EPNdB) and largest for the advanced design CRP (11.3 EPNdB).

Minimizing the tip-vortex interaction and decreasing the strength of potential field and viscous wake interactions by reducing the rear-rotor diameter, increasing the rotor-rotor spacing demonstrated acoustic benefits of around 9 EPNdB at both flyover and sideline observer locations. These benefits indicate that the advanced design CRP can meet Stage 4 noise restrictions with a margin of 8.9 EPNdB averaged over the flyover and sideline noise certification conditions. It should be noted that a second design iteration should be carried out to further assess the cruise aerodynamic performance of the advanced design CRP.

10 Summary and Conclusions

An integrated methodology was developed in order to assess the aerodynamic performance and to investigate the noise challenges associated with advanced propfan powered aircraft configurations. The methodology was validated using an advanced

---

[4]Because of the weight penalties due structural reinforcements, cabin insulation and increased propulsion system weight, the maximum takeoff weight of the CRP aircraft arrangements increased relative to the datum turbofan powered aircraft. This in turn led to slightly higher Stage 4 noise limits for the CRP powered aircraft configurations.

turbofan aircraft configuration for a short to medium range mission. A baseline counter-rotating propfan engine was designed based on information available in the literature. The focus of the acoustic performance assessment was to predict the interaction tones which tend to dominate the noise levels at low-speed operating conditions. The individual contributions of front-rotor wake interaction, aft-rotor upstream influence, hub-endwall secondary flows, and front-rotor tip-vortices to interaction tone noise were dissected and quantified for the first time. Furthermore, the analysis demonstrated that all noise source mechanisms need to be addressed in order to achieve significant noise reductions. A redesign of the baseline CRP was carried out with the goal to reduce interaction tone noise. Minimizing the tip-vortex interaction and reducing wake and upstream influence effects by increasing the rotor-rotor spacing and decreasing the rear-rotor diameter yielded significant interaction noise reductions relative to the baseline design. (The average interaction tone reduction was 7.25 dB in mean SPL computed over the forward and aft polar angle arcs.)

On the aircraft system level, the redesigned CRP demonstrated noise reductions of 9.2 EPNdB and 8.6 EPNdB relative to the baseline CRP aircraft configuration at the FAR 36 flyover and sideline observer locations, respectively. The acoustic assessment suggests that Stage 4 noise limits can possibly be met with advanced open rotor designs.

Future work includes the detailed assessment of the CRP aerodynamic performance at cruise and the investigation of nonuniform inflow, such as, for example, due to a pylon, which can influence the CRP noise and performance characteristics. Finally, in light of higher relative tip Mach numbers at cruise conditions relevant for cabin noise, the CRP noise estimation method can be extended to account for quadrupole noise sources.

Acknowledgment

Nomenclature

A = blade area
B_1, B_2 = front-rotor/rear-rotor blade count
BPF_1, BPF_2 = front-rotor/rear-rotor blade passing frequency
C_P = power coefficient
C_T = thrust coefficient
c_0 = speed of sound in ambient fluid
D, D_1, D_2 = average/front-rotor/rear-rotor diameter
EPNL = effective perceived noise level
f = frequency
F_i = force per unit area on blade surface in direction i
G = Green's function
h = flight altitude
J = advance ratio
k = loading harmonic order
k_m = wavenumber
M = flight Mach number
M_N = Mach number normal to blade surface
M_t = tip Mach number
m, n = harmonic of blade passing frequency

N, N_1, N_2 = average/front-rotor/rear-rotor shaft speed
N_{LP} = low-pressure spool rotational speed
OASPL = overall sound pressure level
P_{Tm}, P_{Lm} = thickness/loading noise at harmonic m
p' = acoustic pressure disturbance
p_t = stagnation pressure
r_t, r_h = tip radius/hub radius
S = amplitude radius
SPL = sound pressure level
T = time limit for acoustic analogy integrals
T_1, T_2 = period of front-rotor/rear-rotor revolution
t = time
V_N = velocity normal to blade surface
$\boldsymbol{x}$ = observer coordinates, x, y, z
x/D_1 = rotor-rotor axial spacing (defined as distance between front- and rear-rotor stacking lines)
$\boldsymbol{y}$ = source coordinates, x_0, y_0, z_0
β_1, β_2 = front-rotor/rear-rotor blade angle setting at 75% span, measured from the tangential direction
γ = specific heat ratio
η_P = propulsive efficiency
θ = polar directivity angle
ρ_0 = free stream density
σ = phase radius
τ = source time
φ = blade sweep
φ_S = tangential source coordinate
φ_{ref} = blade position reference angle
φ_0 = tangential blade coordinate in source integration
Ω = rotor rotational speed

References

[1] Hager, R., and Vrabel, D., 1988, "Advanced Turboprop Project," NASA Technical Report No. SP-495.
[2] Strack, W., Knip, G., Weisbrich, A., Godston, J., and Bradley, E., 1982, "Technology and Benefits of Aircraft Counter-Rotation Propellers," NASA Technical Report No. TM-82983.
[3] Groeneweg, J., and Bober, L., 1988, "NASA Advanced Propeller Research," NASA Technical Report No. TM-101361.
[4] Metzger, F., 1995, "A Review of Propeller Noise Prediction Methodology 1919–1994," NASA Technical Report No. CR-198156.
[5] Hanson, D., 1983, "Compressible Helicoidal Surface Theory Propeller Aerodynamics and Noise," AIAA J., **21**, pp. 881–889.
[6] Hanson, D., 1985, "Noise of Counter-Rotation Propellers," J. Aircr., **22**(7), pp. 609–617.
[7] Zachariadis, A., and Hall, C., 2009, "Application of a Navier–Stokes Solver to the Study of Open Rotor Aerodynamics," Paper No. GT2009-59332.
[8] Polacsek, C., and Barrier, R., 2007, "Numerical Simulation of Counter-Rotating Fan Aeroacoustics," AIAA Paper No. 2007-3680.
[9] Stuermer, A., and Yin, J., 2009, "Low-Speed Aerodynamics and Aeroacoustics of CROR Propulsion Systems," AIAA Paper No. 2009-3134.
[10] Hanson, D., and Parzych, D., 1993, "Theory for Noise of Propellers in Angular Inflow With Parametric Studies and Experimental Verification," NASA Technical Report No. CR-4499.
[11] Magliozzi, B., Hanson, D., and Amiet, R., 1991, "Propeller and Propfan Noise," NASA, Langley Research Center, Aeroacoustics of Flight Vehicles: Theory and Practice, Volume 1: Noise Sources, pp. 1–64.
[12] Majjigi, R., Uenishi, K., and Gliebe, P., 1989, "An Investigation of Counter-rotating Tip Vortex Interaction," NASA Technical Report No. CR-185135.
[13] Janardan, B., and Gliebe, P., 1991, "Acoustic Power Level Comparisons of Model-Scale Counterrotating Unducted Fans," AIAA Paper No. 1991-0595.
[14] Woodward, R., and Gordon, E., 1988, "Noise of a Model Counterrotation Propeller With Reduced Aft Rotor Diameter at Simulated Takeoff/Approach Conditions (F7/A3)," AIAA Paper No. 1988-0263.
[15] Brookfield, J., and Waitz, I., 2000, "Trailing-Edge Blowing for Reduction of Turbomachinery Fan Noise," J. Propul. Power, **16**(1), pp. 57–64.
[16] Peters, A., 2010, "Assessment of Propfan Propulsion Systems for Reduced Environmental Impact," MS thesis, Massachusetts Institute of Technology, Cambridge, MA.
[17] McCullers, L., 1984, "Aircraft Configuration Optimization Including Optimized Flight Profiles," *Recent Experiences in Multidisciplinary Analysis and Optimization, Part 1*, NASA, Langley Research Center.
[18] Kurzke, J., 2007, GasTurb 11 User Manual.
[19] Drela, M., 2007, *RVL (Rotor Vortex Lattice) and RAXAN (Rotor Axisymmetric*

Analysis) User Manuals, Massachusetts Institute of Technology, Cambridge, MA.

[20] Numeca FINE/Turbo 8.7-3, 2009, www.numeca.com

[21] March, A., 2008, "Influence of Low-Speed Aerodynamic Performance on Airport Community Noise," MS thesis, Massachusetts Institute of Technology, Cambridge, MA.

[22] ESDU Aircraft Noise Series, 2007, www.esdu.com

[23] Hannigan, T., and Wainauski, H., 1991, "Wind Tunnel Results of Counter Rotation Propfans Designed With Lifting Line and Euler Code Methods," AIAA Paper No. 1991-2499.

[24] Chapman, D., Fleury, R., and Smith, D., 1989, "Testing of the 578-DX Propfan Propulsion System," AIAA Paper No. 1989-2581.

[25] Goldstein, M., 1974, "Unified Approach to Aerodynamic Sound Generation in the Presence of Solid Boundaries," J. Acoust. Soc. Am., **56**(2), pp. 497–509.

[26] Hanson, D., and Fink, M., 1979, "The Importance of Quadrupole Sources in Prediction of Transonic Tip Speed Propeller Noise," J. Sound Vib., **62**(1), pp. 19–38.

[27] Spalart, P., and Allmaras, S., 1992, "A One-Equation Turbulence Model for Aerodynamic Flows," AIAA Paper No. 1992-0439.

[28] Woodward, R., 1990, "Noise of Simulated Installed Model Counterrotation Propeller at Angle-of-Attack and Takeoff/Approach Conditions," AIAA Paper No. 1990-0283.